Special Collection

FeTiO₃ as Anode Material for Sodium-Ion Batteries: from Morphology Control to Decomposition

Gabriele Brugnetti, Michele Fiore, Roberto Lorenzi, Alberto Paleari, Chiara Ferrara,* and Riccardo Ruffo[a]

Ilmenite, general formula FeTiO₃, has been proposed as possible conversion anode material for lithium- and sodium-ion batteries, with theoretical capacity of 530 mAhg⁻¹. Experimentally, the observed specific capacity for pristine ilmenite is far away from the theoretical value; for this reason, the control of morphology via alkaline hydrothermal treatment has been proposed as possible strategy to improve the electrochemical performance. At the same time FeTiO₃ is prone to react with sodium and potassium hydroxide, as already demonstrated by studies on the degradation of ilmenite for the extraction of TiO₂. In this paper we demonstrate that the alkaline treatment does not induce a morphological modification of the FeTiO₃ powders but involved the degradation of the precursor material with the formation of different phases. A complete physico-chemical and electrochemical characterization is performed with the aim of correlating structural and functional properties of the obtained products.

1. Introduction

The continuous and urgent demand for more performing, cheap and environmentally friendly electrochemical devices promotes the research for new materials. In the field of electrochemical energy storage, sodium-ion-based devices (batteries and capacitors) are driving the research activities as they can potentially overcome the main problems related with lithium-ion based systems in terms of cost and sustainability. At the same time, the technology of sodium-ion batteries (SIBs) is still not mature, particularly the development of new electrode components represents a crucial issue. Many different materials have been investigated ranging from alloy, to carbon-based systems, and transition metal oxides.[1–5] Between them ilmenite (FeTiO₃), has been recently proposed as possible negative electrode material for lithium and sodium-ion batteries[6–8] and for sodium-ion supercapacitor[9] thanks to the high theoretical capacity, chemical stability and low cost. Similarly to Fe₂O₃, FeTiO₃ is considered as a conversion-type material, with possible electrode reaction FeTiO₃ + 3Li⁺ + e⁻ → Fe + LiTiO₂ + Li₂O.[6] The major drawbacks on these conversion materials are the low electrical conductivity together with significant volumetric expansion associated with the ionic insertion/de-insertion processes. To improve the overall electrode reaction efficiency one of the most valuable strategy is the control of morphology. Reduced particle size and high specific superficial area can be obtained during the synthesis following wet

chemistry routes. Although synthesis of ilmenite with specific morphology have been reported,[10–16] the bottom up approach may not represent the best preparation method as FeTiO₃ is a cheap natural product and already commercially available. For this reason, the top down approach has been followed: small particles were obtained by ball milling processes followed by hydrothermal treatment leading to a significant modification of the particle's morphology and the appearance of nano-flower like structures. The good electrochemical performances observed for nano-flower like material have been ascribed to the peculiar morphology in case of both sodium-ion supercapacitor and LIBs.[6,9] Subsequent works confirmed the improved electrochemical properties (improved capacity, cycling stability) of modified ilmenite samples with respect to pristine ilmenite that does not show satisfying results.[7,8]

Beside these possible advanced applications, ilmenite has been exploited for decades as one of the most abundant Ti-containing mineral and every year an amount of ~5 million metric tons of ilmenite ores are processed for extraction of TiO₂ and/or Ti.[17] Among the several different possible industrial and laboratory procedures for the ilmenite degradation, recently alkaline processes have been proposed.[18] Ilmenite powders treated in NaOH or KOH 10 M solution in the temperature range 150–220°C react giving sodium titanate and iron oxide phases; subsequent acid leaching allows to obtain pure TiO₂ powders.[18,19] On the base of these considerations, it is thus essential to pay special attention to the control of experimental conditions of the hydrothermal treatment as a method to tune the morphology, as ilmenite is prone to react and degrade under basic environment.

The aim of this work is to explore and characterize the bottom up procedure that can lead to a morphology control of ilmenite powders, namely the ball milling and hydrothermal treatments. A detailed investigation of the effect of the ball milling and hydrothermal treatments on the structure and actual composition of the final products is performed together

[a] G. Brugnetti, Dr. M. Fiore, Dr. R. Lorenzi, Prof. A. Paleari, Dr. C. Ferrara, Prof. R. Ruffo
Department of Materials Science, University of Milano Bicocca
via R. Cozzi 55, I-20125 Milan, Italy
E-mail: chiara.ferrara@unimib.it

ChemElectroChem

Articles
doi.org/10.1002/celc.202000150

Chemistry Europe
European Chemical
Societies Publishing

with the electrochemical characterization of the different phases. The multi-technique approach (with the combined use of TGA-DTA, XRD, ICP, SEM EDX) allowed us to determine the degradation mechanism and reaction under the explored experimental conditions. The subsequent electrochemical tests coupled with ex-situ XRD measurements and operando Raman data confirmed the ilmenite electrode reaction and demonstrate its reversibility.

2. Results and Discussion

2.1. Preliminary Information

Prior the presentation on the experimental data some structural features of ilmenite are here recalled to simplify the subsequent discussion of the results. $FeTiO_3$ ilmenite is a wide bandgap (2.6–2.9 eV) anti-ferromagnetic semiconductor with a structure derived from the hematite system. Ilmenite–hematite constitutes a solid solution and members of this systems are often observed as natural minerals associated with igneous and metamorphic rocks. Fe_2O_3 hematite crystallizes in R-3c corundum structure in which Fe ions occupy octahedral sites forming layers in the (001) plane. Ilmenite emerges from the hematite structure, with a change in symmetry to R-3, due to the ordering of Ti cations substituting Fe (according to the scheme $2Fe^{3+} \rightarrow Fe^{2+} + Ti^{4+}$) in alternating octahedral layers along [001] direction,[20] as reported in Figure 1.

The magnetic structure and the ordering effect in the cation sublattice have been subject of detailed investigation [ref. 20 and references therein], the discussion of these aspects goes beyond the scope of this work. Ilmenite is one of the mineral responsible in determining the natural Earth's magnetism together with hematite. Moreover, is the most abundant Ti-containing mineral used for the production of TiO_2.[21] Natural occurring ilmenite is often associated with variable amount of impurity (mainly Cr, Mg, Mn, V, Al, Si, Ca rare earth depending
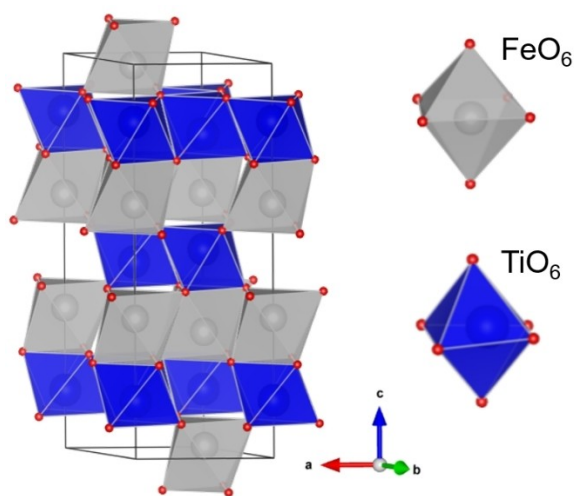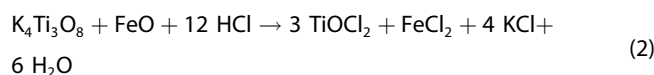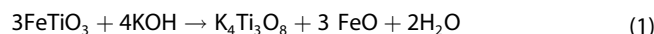
on the geological history),[21,22] variable content of titanium ranging from 40 to 65 % (and the formula can be expressed as $FeTiO_3:TiO_2$) and different possible combination of Fe^{2+}/Ti^{4+} or Fe^{3+}/Ti^{3+}.[10,15] Commercial extraction of titania from ilmenite dates back the 1920's and nowadays the world production is about 5.3 million metric tons with continuous growing of the worldwide TiO_2 demand, while the ilmenite natural reserves estimated for 800.000 tons.[17] Several industrial procedures are applied for the production of TiO_2 (mainly sulphate and chloride process at high temperature) and Ti metal (Kroll process).[19,21,23,24] Due to the huge volume of production, new less energetic and cheap methods have been developed for the titania extraction. In particular, recently the soda ash roasting and treatments in basic conditions (KOH, NaOH) have been reported.[18,19,25] The production of pure titania follows two steps: initially the reaction with the alkaline hydroxide degrades the ilmenite into a sodium titanate and iron oxide. In a subsequent step TiO_2 is recovered from the sodium titanate by acid leaching following the scheme [Reactions (1) and(2)]:

$$3FeTiO_3 + 4KOH \rightarrow K_4Ti_3O_8 + 3\,FeO + 2H_2O \tag{1}$$

$$K_4Ti_3O_8 + FeO + 12\,HCl \rightarrow 3\,TiOCl_2 + FeCl_2 + 4\,KCl + 6\,H_2O \tag{2}$$

The separation of Ti-rich materials from Fe residues is claimed to be facilitated by the insoluble nature of the Ti based compound and, on the contrary, to the solubility in water of the Fe-containing species.[22] In agreement with Liu et al..[18] Reaction (1) was proposed also by another group[19] who used NaOH in solid state reaction instead of hydrothermal treatment with KOH obtaining the same results. Jardim et al. who performed a hydrothermal treatment with 10 M NaOH obtained a different degradation product, namely $Na_{x-y}H_yTi_{2-x}Fe_xO_4$ with lepidocrocite structure.[26] In all these works the starting product was natural ilmenite (used without further purification) obtained from different geographical regions and containing different impurities in terms of quantity and composition.[27] Other authors report the reactivity of ilmenite in NaOH solution under hydrothermal conditions, resulting in a new nonstoichiometric compound containing Na, Ti and Fe[28] but conditions of the hydrothermal treatment have not been specified. From the available data it seems that the results of the degradation process depend on the actual composition of the starting material (the nature and the amount of the impurities, the actual Fe:Ti ratio), the particle size of the starting powders, the strength of the conditions (concentration of the hydroxide, temperature, duration of the treatment) and seems to be difficult to replicate the composition of the degraded products.

On these bases in this work we considered ball milling process and hydrothermal treatment as two possible ways for the reduction of the powder particles size and the morphology control. To avoid the variability introduced by the presence of impurities and Fe:Ti ratio, the ilmenite considered in this work is characterized by high purity (99.9 %); particular attention has been devoted in reducing the particle size of the powders and in controlling the experimental conditions of the ball milling

Figure 1. Ilmenite structure, Fe ion in gray, Ti ion in blue, O ion in red together with FeO_6 and TiO_6 units.

ChemElectroChem

Articles
doi.org/10.1002/celc.202000150

**Chemistry
Europe**
European Chemical
Societies Publishing

and hydrothermal treatments, as described in the following section.

2.2. Ball Milling Treatment

The commercial powders were ball milled prior the electrochemical test and/or the hydrothermal treatment to reduce the grains dimension. Both rotation speed and milling time have been varied to identify the best conditions to obtain pure nano-sized ilmenite; results of XRD analysis for different samples are reported in Figure 2. The effect of the ball milling treatment on the particle size has been evaluated monitoring the peaks broadening, in agreement with the Scherrer equation. With low rotation speed 300 rpm for 12 hours only partial size reduction is obtained (sample FTO_BM312) while increasing the rotation
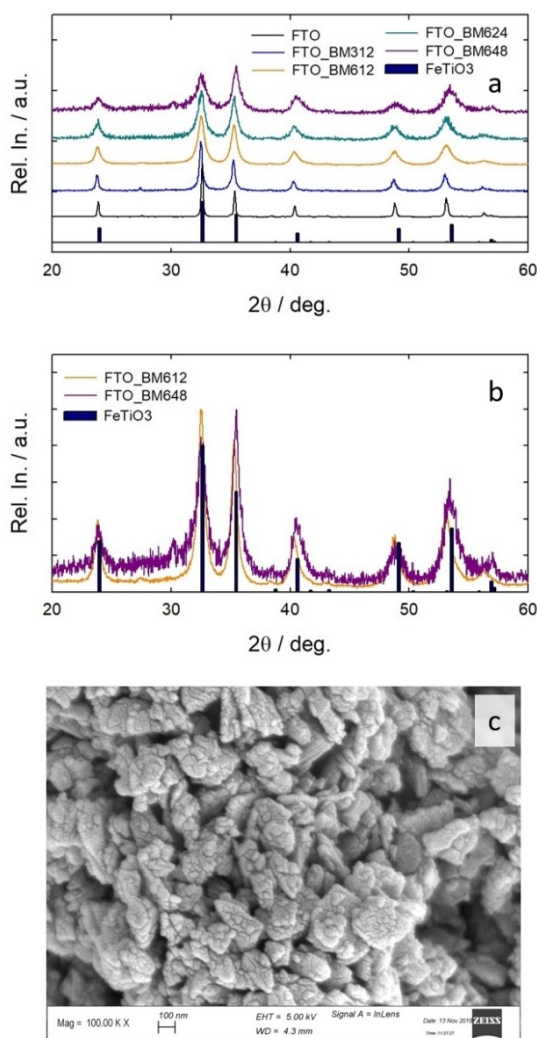

Figure 2. a) XRD of commercial ilmenite (black) and samples ball milled at 300 rpm for 12 h (blue) and at 600 rpm for 12 h (orange) 24 h (green) and 48 h (purple) together with Bragg position for ilmenite structure (JCPDS 01-075-1212); b) Direct comparison of patterns obtained for samples milled at 600 rpm for 12 and 48 h; c) SEM image for the sample ball milled for 12 h.

speed at 600 rpm for the same treatment time allows to significantly reduce the grain size (sample FTO_BM612). A further increase in the duration of the treatment up to 24 hours does not lead to any significant difference in peaks position and/or broadening (sample FTO_BM624). On the contrary an increase of the milling time up to 48 h (sample FTO_BM648) results in a shift of only some of the ilmenite reflections (see for examples peaks at 41°, 54° and 57° in Figure 2a) that are also affected by anisotropic broadening and inversion of the intensities together with the appearance of a new reflection centered at 30°; a modification of the background is also observed (see Figure 2b). These effects are compatible with the introduction of a strain along particular directions and/or changes in the staking of the layered arrangement of the ilmenite structure and in general with the disordering of the structure.

All the powders used for the following hydrothermal steps and electrochemical tests in this work have been obtained with ball milling treatment of 12 h at 600 rpm as no significant changes in the particle size can be estimated between the sample obtained at 12 h and those obtained at 48 h while on the contrary this last one is affected by induced strain or defects in the stacking. In previous report the ball milling treatment was pushed up to 150 hours[9] but comparison with results of the present work is not possible due to the different milling system. From SEM images of the sample obtained at 600 rpm at 12 h (Figure 2c) it is possible to estimate the size of the agglomerates in the range 100–200 nm, probably constituted by smaller particles (cracked appearance due to the conductive gold sputtered layer), in good agreement with the values obtained from the analysis of the diffraction broadening. Particles appear with a wide distribution of shapes, no significant anisotropies are evidenced, and no ordered morphology is detected, in good agreement with data previously reported.[9]

2.3. Hydrothermal Treatment

A first attempt to prepare a nano-structured ilmenite sample has been performed following the procedure previously reported using a Schott bottle as reactor vessel, NaOH 2 M for 2 h maintained at 120 °C;[9] corresponding XRD patterns and SEM images obtained for this sample are reported in Figure S1. A significant change of the morphology can be observed as the powders of the FTO_Schott samples are constituted by lamellar components with average dimension of ∼100 nm but at the same time we were not able to replicate the literature data as the peculiar well organized nano-flowers morphology was not evident for any portion of the sample. Nevertheless, the XRD pattern of the FTO_Schott sample presents an intense extra peak at ∼9°, as evident from Figure S1, suggesting the appearance of a secondary phase after the hydrothermal treatment.

Despite this evidence of the degradation of the sample, the characterization of the FTO_Schott material have been completed with the collection of galvanostatic tests at different C-

ChemElectroChem

Articles
doi.org/10.1002/celc.202000150

Chemistry
Europe
European Chemical
Societies Publishing

rates and results have been compared with the profiles obtained for the commercial FTO and FTO_BM612 samples (see Figure S1). The cyclability of the FTO_Schott sample is significantly improved respect to the ball milled and commercial ilmenite and also respect to results previously reported.[6] The capacity obtained for FTO commercial powder is low compared to the theoretical value (~ 60 mAhg^{-1}) and shows only a weak dependence with the C-rate. On the contrary, the FTO_BM612 and FTO_Schott samples can deliver higher specific capacity values at low C rate while at higher C values the specific capacity values drop. However, the performances of the FTO_Schott sample are always better respect to those of the FTO and FTO_BM612 samples. It is thus essential to understand the correlation between the electrochemical performances, the composition, and the morphology of the hydrothermally treated sample. Motivated by this aim, different samples have been prepared following the hydrothermal procedure trying to minimize the presence of impurities. As the EDX analysis obtained for the FTO_Schott sample reveal a significant contamination of the powders (Si, Ca, Mg, Na) probably coming from the deterioration of the reaction vessel, all the subsequent samples have been prepared in a Teflon autoclave under the same experimental conditions (continuous stirring, sealed vessel with the same filling factor, thermostatic heating). A series of samples have been prepared prolonging the duration of the hydrothermal treatment (see the complete list in Table S1); the variation of other parameters (temperature, NaOH concentration) has been discarded as stronger conditions can lead to a sever decomposition of the ilmenite powder, as described in the previous section.

The XRPD patterns obtained varying the duration of the treatment are presented in Figure 3a. Peaks attributed to ilmenite can be detected in each pattern but at the same time a strong new reflection appears at $\sim 10°$, becoming dominating already for short treatment time. Other reflections are observed at 28°, 33° and 35°. As ilmenite was the only phase present during the treatment and careful washing was performed at the end of the procedure, the appearance of new reflections is ascribed to the decomposition of ilmenite due to the presence of NaOH, as already reported. Although it was not possible to associate these reflections to any of the already reported decomposition products discussed in the previous section, the global decomposition mechanism is in good agreement with literature data suggesting that the ilmenite under basic conditions undergoes a phase separation resulting in iron rich and titanium rich compounds.[18,19,22]

Under the experimental condition here reported, the extra-peaks can be associated to the presence of a mixture of phases; the main constituent can be identified as a layered titanate of general formula $(Na/H)_2Ti_2O_5*H_2O$ and hematite Fe_2O_3 (see Figure 3b). Hematite structure is strictly correlated to that of ilmenite resulting in similar reflections (see Figure 3b) as discussed in the Preliminary Information paragraph. Layered titanates and titania nanotubes are generally obtained from hydrothermal treatment of TiO_2 with concentrated NaOH at moderate temperature[29–33] under conditions very similar to those considered in the present work. A wide variety of layered
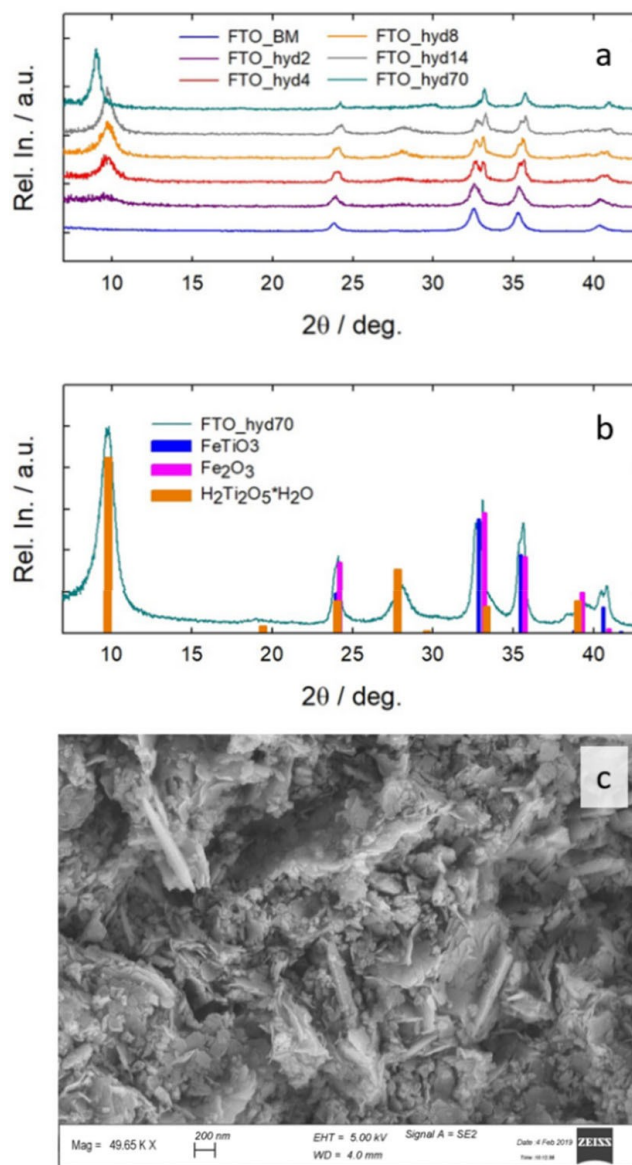

Figure 3. a) XRD patterns for samples prepared in autoclave varying the treatment duration (2–70 hours) and pattern for the FTO_BM612 sample as reference; b) pattern for the FTO_hyd70 samples together with the reference Bragg peaks for the FeTiO$_3$ (JCPDS card 01-075-1212), Fe$_2$O$_3$ (JCPDS 33-0664) and H$_2$Ti$_2$O$_5$*H$_2$O (JCPDS 47-0124) structures; c) SEM image obtained for the FTO_hyd70 samples.

and nanotubes titanates have been reported, corresponding to different stoichiometry and compositions ($H_2Ti_3O_7$,[29] $H_xTi_{2-x/4-x/4}O_4$,[30] $Na_2Ti_2O_4(OH)_2$,[31] $H_2Ti_4O_9$)[34] often undetermined.[32,33] These systems are generally composed by layers of TiO_6 units stacked along c direction and spaced by layers containing H^+, OH^-, H_2O, Na^+ ions; both composition and structure strongly depend on the synthesis and washing conditions. For most of these systems the crystal structure has not been reported due to the complexity of the hierarchical layered structure. The reflections observed in this work for the hydrothermally prepared samples are affected by a significant broadening, relatable with the non-completely crystalline nature of the system and are compatible with different nanotubes poly-

ChemElectroChem

Articles
doi.org/10.1002/celc.202000150

Chemistry Europe
European Chemical
Societies Publishing

morphs and species mentioned above. Due to the low level of crystallinity of the phases in the mixtures it is not possible to perform a detailed quantitative analysis of the diffraction patterns. The position of the peak at ~8–10° is strongly dependent on the duration of the hydrothermal treatment and washing conditions. A sharp correlation between the content of the layers (Na$^+$, H$^+$; H$_2$O, OH$^-$) and the position of this peak (related to the elongated dimension of the unit cell) has been described and exploited for the evaluation of the actual composition of the system.[35,36]

The SEM EDX data acquired for the same compositions clearly show the effect of the hydrothermal treatment on the morphology of the powders with the appearance of lamellar formations and agglomerates resembling the nano-flowers systems previously reported[6,9] (see Figure 3c). The composition analysis reveals that on average no significant variation from Fe:Ti 1:1 stoichiometry is detected, in good agreement with previous report[9] and locally only small variations (in the order of ~10%) are observed.

The appearance of lamellar and nano-flower like particles is thus to be ascribed to the degradation of the sample with the formation of new phases and not to a purely morphological effect of the hydrothermal treatment on the ilmenite powders.

These results are confirmed also by ICP analysis performed on different portion of the solid sample FTO_hyd70 and the residual waters at different stages of washing with deionized water (corresponding at different pH values). The analysis (see Table S2) highlight as only a small loss of Fe from the powder to the solution can be observed under the experimental conditions (quantified as lower than 4%), differently from what reported for the degradation of ilmenite under basic conditions with the formation of soluble iron complexes. It must be stressed that in our study the starting material was FeTiO$_3$ with purity >99%, while previous studies on the hydrothermal treatment of ilmenite for Ti extraction were obviously dealing with natural ores with a wide variety of impurities in terms of amount and composition. As already discussed, these impurities have been observed to significantly affect the mechanism and products of the degradation process as similar hydrothermal conditions result in very different products starting from different natural ores.[29–33] The combined analysis of XRD, ICP, and SEM-EDX data suggest that the FTO_hyd70 sample has, on average, the same nominal Fe:Ti composition of the precursor materials but is composed by different crystal phases. The identification of the degradation phases is further supported by the TGA/DTA profile obtained for the FTO, FTO_BM612, and FTO_hyd70 reported in Figure S2a. While in the explored temperature range (25°-1000°C) the FTO and FTO_BM612 sample do not present significant weight loss and/or thermal phenomenon on the contrary the profile of FTO_hyd70 sample shows two distinct weight losses below 400°C and two thermic processes in the 800°–1000°C range. The TGA features can be ascribed to structural changes in the (Na/H)$_2$Ti$_2$O$_5$*H$_2$O components with the first part related to the loss of hydration water molecules (25°–150°C) and interlayers H$^+$/H$_2$O/H$_3$O$^+$ species (150°- 400°C), as already reported for similar layered systems[37,38] leading to the formation of sodium rich layered

titanates (possible formula derived from the former one: NaTi$_2$O$_5$). The species present melting temperature in the range for which DTA curve shows endothermic features (800°-1000 C°),[39] supporting the idea of dehydration and subsequent melting of layered sodium titanates. This trend is compatible with the average composition of the titanate evaluated by the EDX data; Ti:Na ratio is 1:0.25, compatible with partial substitution of H with Na during the hydrothermal treatment. Ex-situ XRD data acquired for the FTO_hyd70 sample treated up to 900°C (see Figure S2b) further validate this hypothesis as the titanate main reflection (~8–10°) undergoes a shift at higher angles in the range 25°–400°C related to water loss from the intra-layers water molecules; treatment at highest temperature involves the collapse of the layered structure followed by phase transitions and reaction with the other species present in the samples with the formation of different sodium titanate and sodium iron titanate phases. At higher temperature the sodium titanate and the remaining hematite start reacting forming again ilmenite compound. Based on the XRD, DTA-TGA, ICP, and EDX analysis the FTO_hyd70 estimated composition is 1:1 molar ratio of Fe$_2$O$_3$ and (H/Na)$_2$Ti$_2$O$_5$*H$_2$O.

Based on the detailed physicochemical characterization of the FTO_BM and FTO_hyd series of samples it is finally possible to rationalize and differentiate the effect of the ball milling and hydrothermal treatment. While with the former it is possible to reduce the particle size of the powders under mild milling conditions, the latter induces a degradation of the initial compound to Ti and Fe rich phases; the observed changes in the particles morphology must be associated to the formation of these new phases that cannot be neglected when the material is tested for electrochemical applications. It must be stressed that the degree and mechanism of the decomposition are strongly affected by the level and nature of the impurities in the starting ilmenite powders.

The FTO_BM612 and FTO_hyd70 samples have been selected for further electrochemical tests and allowed us to explore the two end member cases: pure ilmenite characterized by nano dimension of the powder particles (FTO_BM612 sample) and fully degraded ilmenite, constituted mainly by layered titanate and hematite-based phases (FTO_hyd70 sample).

Quasi-equilibrium PCGA curves of the cells assembled with FTO_BM612 and FTO_hyd70 materials are reported in Figure 4a and 4d. The first cathodic scan of FTO_BM612 is significantly different respect to the profiles reported for the successive cycles, showing an irreversible reaction at ~0.45 V (sharp peak in Figure 4b). On the contrary, the anodic profiles are stable upon cycling, indeed, two broad peaks are detected at ~0.9 and ~1.7 V. Similar differences between the cathodic/anodic profiles have been observed also for the Co$_3$O$_4$ conversion anode material.[40] The strong irreversibility of the first cycle is typically of conversion electrode materials,[40–42] and similar behavior has already been observed for ball milled ilmenite tested vs metallic Li and related to the possible electrode reaction FeTiO$_3$ + 3Li$^+$ + e$^-$ → Fe + LiTiO$_2$ + Li$_2$O.[6]

The profiles of the FTO_hyd70 sample (see Figures 4d and 4e) are significantly different from those of FTO_BM612 based

ChemElectroChem

Articles
doi.org/10.1002/celc.202000150

Chemistry Europe
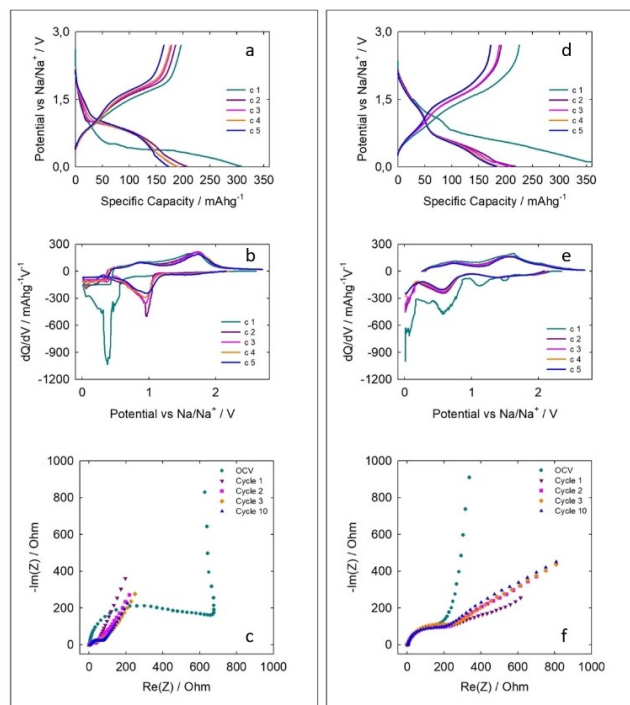European Chemical
Societies Publishing

Figure 4. From the top, PCGA profiles, specific capacity, and EIS profiles obtained in 5 −10 cycles for cell assembled with a–b–c) FTO_BM612 and d–e–f) FTO_hyd70 active materials.

Figure 5. GCPL profiles and specific capacity as function of the cycles number for cell assembled with a–b) FTO_BM612 and c–d) FTO_hyd70 active materials.

cell. The profile difference between the first and subsequent cycles is much less pronounced, supporting the idea that the main component in the FTO_hyd70 sample is the layered titanate behaving as insertion type material, indeed, the position of the cathodic and anodic peaks is different respect to those observed for the FTO_BM612 sample. This type of evolution of the profiles with cycling have been observed for similar layered titanate systems.[43–45]

The comparison of the PCGA profiles supports the idea that the two samples are different in terms of crystal phase composition, resulting in different electrochemical behaviours.

These results are also confirmed by galvanostatic cycling with potential limitation (GCPL) profiles reported in Figure 5. The first sodiation of FTO_BM612 differs from the following ones in both capacity and potential profile, due to the presence of the first conversion step. The sample shows a Coulomb efficiency of 62% at the first cycle which then increases to about 95%. The specific capacity is around 150 mAh g^{-1} at the first anodic desodiation and stabilizes to 125 mAh g^{-1} after 5 cycles. The average anodic and cathodic potentials are 1.51 and 0.89 V, respectively. A larger irreversibility in the first cycle is observed also for FTO_hyd70, however the first cathodic potential profile is similar to the following ones. In this case, the nanometric morphology leads to larger surface area and thus increased electrolyte decomposition. The electrochemical performances of the sample are similar with those of the milled sample in term of specific capacity but differ for the average potentials (0.74 and 1.40 for the cathodic and anodic process, respectively). These results are further supported by the electro-
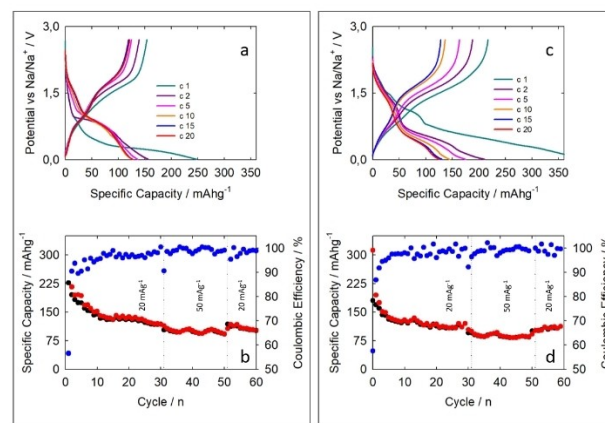
chemical impedance spectroscopy (EIS) data (Figure 4c and 4f). For a more meaningful comparison of the results, the spectra were acquired over several charge and discharge cycles in the de-sodiated state (end of the anodic branch) after waiting for OCV stabilization. The Nyquist impedances of compound FTO_BM612 show a substantial change following the first charge and discharge cycle, while remaining substantially unchanged in the subsequent 9 cycles. The change concerns both the low frequency characteristics, where it passes from a capacitive to a diffusive system, and the response to higher frequencies, where the interface resistance varies from about 500 to 40 Ω and then remains unchanged in the subsequent cycles. On the other hand, the FTO_hyd70 sample shows a very similar spectrum from the first measurement and Nyquist impedances vary only for the diffusive part, while the interface resistance remains substantially unchanged (around 275 Ω). The observed cycling stability reported in Figure 5b and d of the two materials up to 60 cycles further support the idea of different electrode reactions. The capacity retention of the FTO_BM612 sample calculated on 60 cycles is ~45% and the specific capacity value is not stabilized yet while for the FTO_hyd70 the capacity retention is significantly higher (~62%) and the specific capacity is almost stabilized after 30 cycles (capacity retention calculated after cycle 30 for the FTO_BM612 sample ~87% and ~94% for the FTO_hyd70 sample). The poor capacity retention of the FTO_BM612 is typical of a conversion type electrode material, the poor cycling performance are generally associated with the mechanical degradation of the anode material due to the volume variations associated to the reaction mechanism; this effect has already been observed for iron based oxides both in LIBs and SIBs.[46–49] The higher capacity retention observed for the FTO_hyd70 sample is in turn related to the electrochemical activity of the layered titanate as insertion like anode material. The layered structure characterized by huge interlayer distance[31–34] allows for facile insertion/de-insertion of Na ions and thus in improved stability upon cycling respect to a conversion-type anode material, as already reported for similar

ChemElectroChem

Articles
doi.org/10.1002/celc.202000150

**Chemistry
Europe**
European Chemical
Societies Publishing

systems.[50–52] The performance of the FTO_hyd70 are not directly comparable with the highly promising literature data for layered titanate systems[43–45,50–52] as in our case the layered titanate is only a fraction of the active material, in which also Fe_2O_3 is present. Moreover, the formulation of the anode mixture in terms of binder and relative ratio of carbon:binder:active materials has not been optimized to obtain the best possible performance, goal that was out of the scope of the present study.

In conclusion, the electrochemical studies presented in Figure 4 and 5 highlight the differences between FTO_BM612 and FTO_hyd70 samples, confirming the modification in the phase compositions of the two materials. The FTO_BM612 performances are compatible with the conversion reaction previously reported for ilmenite phase[6] and generally the profile evolution upon cycling is similar with the trend already observed for other oxides considered as conversion type anode materials, e.g. Co_3O_4[40,53] and Fe_2O_3[42,54] and generally of transition metal oxide materials considered as anodes[46–49] On the contrary, the electrochemical behavior of FTO_hyd70 sample can be associated with a insertion like mechanism as already observed for similar systems.[43–45,50–52] A detailed analysis of the FTO_hyd70 curves is not straightforward as the actual composition of the sample is in turn not clear; while the different degradation products have been identified, it was not possible to perform quantitative analysis and determine the relative ratio of the different phases. As already stated, the FTO_hyd70 PCGA and GCPL profiles are typically observed for insertion materials and other layered titanate systems;[43–45] thus, the sodium titanate seems to be the active component in the mixture. The Fe_2O_3 hematite (the other phase identified in the FTO_hyd70 sample), is also electrochemically active as already reported.[54,55] It must be considered that the composition of the active material, in terms of selection of carbon source and binder and relative amount between the different components, is not optimal for the detection of the electrode activity of hematite particularly considering the low carbon content of the present composition (10%) respect to the amount commonly used (30%) necessary to overcome the low electrical conductivity of Fe_2O_3.[54]

To confirm the FTO electrode reaction and its reversibility, operando Raman measurements have been collected on a working cell and coupled to GCPL experiment. Due to the complexity of the system, the impossibility to clearly determine the composition and the number of different phases, the FTO_hyd70 was not considered for this analysis and only the FTO_BM612 sample was further investigated.

Results of the combined operando Raman-GCPL analysis are reported in Figure 6. The Raman spectra of the assembled cell is the result of the superposition of two contributions, from the electrolyte and from ilmenite. The electrolyte spectra (grey line in Figure 6a) presents several peaks, related to the PC solvent (454, 715, and 849 cm^{-1}) and to the ClO^{4-} solute and its derivatives (548, 633, 910, 930 and 957 cm^{-1}), in agreement with literature data.[56,57] The spectrum of the as-prepared cell (black line in Figure 6a) is instead governed by a strong peak at 685 cm^{-1} which matches with the strongest Raman mode in
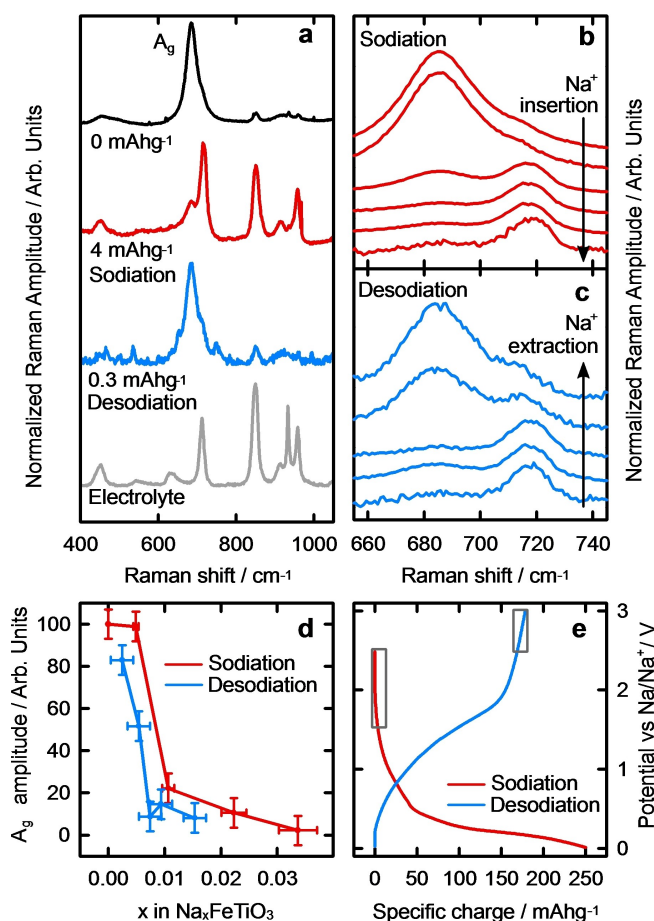

Figure 6. a) Normalized Raman spectra obtained for the optical cell assembled with FTO_BM612 as active material before GCPL experiments (black line), during sodiation (red line) and desodiation (blue line), and Raman spectrum of the electrolyte (gray line). Normalized spectra to the ring deformation mode at 715 cm^{-1} during charging (b) and discharging (c). d) A_g amplitude as a function of the molar fraction of Na$^+$ ions introduced (red points) and extracted (blue points) during charge and discharge, respectively. e) The corresponding GCPL profiles collected on sample FTO_BM612. Spectra in (a), (b) and (c) are upshifted for clarity.

ilmenite.[58] This mode corresponds to the A_g symmetric stretching of the TiO_6 octahedra. Sodiation (red line in Figure 6a) and desodiation (blue line in Figure 6a) processes reversibly alter the intensity of this peak. A detailed analysis of this modification during charging/discharging is summarized in Figure 6b, c and d. First, we used an internal standard signal as normalization peak to overcome possible errors on the determination of the absolute value of the A_g intensity. Specifically, we adopted the ring deformation mode at 715 cm^{-1} as normalization peak. This solvent-related signal is less sensitive to possible variation induced by voltage change with respect to ClO^{4-} anion that may undergo to migration and/or dissociation.

The normalized spectra collected during sodiation and desodiation are reported in Figure 6b and 6c, respectively. The peak profile does not change during the experiment, neither as regard the full width at half maximum nor in the position. These evidences give us a valuable hint about the possible mecha-

ChemElectroChem

Articles
doi.org/10.1002/celc.202000150

Chemistry Europe
European Chemical
Societies Publishing

nisms of the sodium intake and release. On the one hand, the broadness of the ilmenite peak is directly related to its amorphousness[59] while its position strongly depends on the Ti–O bond length as confirmed by high-pressure Raman experiments[60] and spectral modification upon cation substitution.[58,61] On the other hand, the Raman activity of the A_g mode is very sensitive to the local symmetry of the TiO_6 octahedra. Thus, a probable mechanism for sodium insertion involves the intercalation of Na^+ within the Ti–O planes. In this hypothesis, the A_g symmetry is abruptly removed rather than perturbed by minor TiO_6 rearrangements, as encountered in case of tilted, compressed, relaxed and/or amorphous configurations. In fact, this change is reversible (unlikely related to amorphization) and starts to occur at the very early stage of the sodiation process, when Na^+ intercalation cannot cause appreciable long or medium range structural deformations. In Figure 6d the intensity of the A_g mode is reported as a function of the Na^+ molar fraction introduced (or extracted) during battery charge (discharge). During charge, the signal drastically falls when about 0.01 molNa$^+$/molFeTiO$_3$ are incorporated in the system. During discharge, the 80% of the original signal is recovered when about 0.002 molNa$^+$/molFeTiO$_3$ left to full discharge. These values correspond to the ranges 0–10 mAhg^{-1} and 170–180 mAhg^{-1} of the specific charge measured during charge and discharge GCPL experiments (as reported in Figure 6e), respectively. The reversibility of the electrode reaction is further support by the ex-situ XRD pattern collected on the same electrode immediately after the disassembling of the cell; results are reported in Figure S4. The reflections associated to ilmenite compound are almost fully recovered after the electrochemical cycling. Similar dynamics have been registered in repeated measurements (not shown) and agree with that reported in Raman and XRD operando study of Na^+ insertion/extraction in NaFeTiO$_4$ batteries.[62] As a matter of fact, the A_g mode is below the detection limit at 0.033 mol Na$^+$/molFeTiO$_3$. This amount corresponds to an occupancy of ilmenite unit cells by Na ions of 20%. The latter value is sufficient to break the collective motion of TiO_6 octahedra responsible for the observed phonon mode.

3. Conclusions

FeTiO$_3$ has been considered as possible anode material for rechargeable lithium- and sodium- ion batteries based on the possible conversion reaction leading to the formation of metallic iron and alkaline titanate, resulting in high theoretical capacity values.[6,7] The possibility to improve the electrochemical performance of such material controlling the morphology of the powder particles via basic hydrothermal treatment has been proposed.[6] As basic treatment has been proposed as simple and effective route for the degradation of natural ilmenite to recover TiO$_2$, in this study we carefully explored the possible top down approaches to produce nano-sized ilmenite powders, namely ball milling and basic hydrothermal treatments, devoting particular attention in controlling the exper-

imental condition and performing a full structural and electrochemical characterization of the obtained products.

The results obtained from Raman, TGA-DSC, and diffraction analysis indicate that only the mild ball milling treatment allows to obtain FeTiO$_3$ nano powders while maintaining the composition and crystal structure of the pristine materials. On the contrary hydrothermal treatment – for the range of the experimental parameters explored in this study – always leads to a decomposition of the pristine material, accompanied by a change in the morphology. The final electrochemical characterization for the two materials further supports these results.

The degraded sample FTO_hyd70 potential profiles are compatible with an insertion like material; this feature can be associated with the presence of the layered sodium titanate. The second major component of the FTO_hyd70 is hematite, for which no clear evidences of electrochemical activity can be detected due probably to its electrical conductivity combined with the lack of favorable experimental conditions.

FTO_BM612 behaves like a conversion material, characterized by an irreversible step during the first cycle and specific capacity values oscillating around 107–105 mAhg^{-1}, almost stable after 60 cycles, in good agreement with the previously reported data on similar material.[6] Operando Raman measurements confirm the conversion mechanism of the electrode reaction and its reversibility; the crystal structure of ilmenite is retained for insertion of ~0.01% mole of Na, while the features associated with the crystal structure disappear for higher values of inserted sodium ions.

Experimental Section

Sample preparation

Commercial FeTiO$_3$ (FTO) powder purchased by Sigma-Aldrich and stored in Ar filled glovebox ([H$_2$O], [O$_2$] <0.1 ppm) was used as starting material without any further purification. Preliminary check of ilmenite structure and composition has been performed.

Ball milling treatment

Powders have been milled for 12, 24 and 48 h with the use of a Retsch PM 100, equipped with zirconia jars and spheres, prepared and sealed in Ar filled glovebox using spheres with 2 mm of diameter with 10:1 ball: powder weight ratio, 300–600 rpm rotation speed using small amount of ethanol. After the treatment the powders are recovered and characterized.

Hydrothermal treatment

0.3–0.5 g of ball milled powders are insert in Schott bottle or Teflon autoclave with 20–33 ml of 2 M NaOH, corresponding to a NaOH/FeTiO$_3$ molar ratio 1:0.012; temperature was maintained with a thermostatic bath at fixed temperature (120°C) varying the duration of the hydrothermal treatment between 2 and 72 hours; during the treatment vigorous magnetic stirring was maintained. After the treatment the system was cooled down to ambient temperature before subsequent handling of the powders. The recovered powders have been washed with milliq water until neutrality and then dried at 80°C under vacuum overnight.

ChemElectroChem

Articles
doi.org/10.1002/celc.202000150

Chemistry Europe
European Chemical
Societies Publishing

X-ray diffraction

Experimental patterns have been collected on a Rigaku Miniflex 600 in the angular range 5°–70°, with step size 0.02° with the use of Cu K_α radiation. Ex situ measurements have been performed with the same instrument immediately after the disassemble of the cell.

ICP OES analysis

ICP OES have been carried out on powder samples after acid digestion and washing waters after proper dilution, analysis have been collected with ICP-EOS Optima 7000 DV PerkinElmer instrument.

TGA/DTA measurements

The thermal profiles have been acquired with the use of a Mettler Toledo instrument under constant Ar or air flow with heating rate 5 °C/min scan in the range 25°–1000 °C.

SEM/EDX measurements

Scanning electron microscope (SEM) and energy dispersive microanalysis (EDS) have been performed using a Zeiss Gemini 500 instrument.

Electrochemical test

Electrochemical tests have been performed on a VMP3 BioLogic, assembling conventional CR2032 coin cells with metallic Na as counter electrode, active material based on 80:10:10 mixture of FTO:binder:C prepared on Al foil current collector as working electrode and NaClO$_4$ 1 M in PC with 2% FEC as electrolyte (1.5–2.5 mg of active material deposited for each electrode). Super P has been used as carbon source; c–PAA–CMC has been selected as optimal binder for electrochemical tests of conversion electrode materials.[63] The binder has been prepared according to the procedure previously reported,[63] results in very good agreement.

Electrochemical tests have been performed with the use of galvanostatic cycling with potential limitation (GCPL) technique to explore the behavior (reversibility and stabilization upon cycling) of the active material and to determine the specific capacity in 60 cycles with fixed current 20 mAg^{-1} for the first 30 cycles, 50 mAg^{-1} for cycles 31–50 and 20 mAg^{-1} for the 51–60 cycles. Such slow current conditions have been chosen to get the proper material performances, avoiding high current long cycling, a condition that often hides material irreversibility. Potentiodynamic cycling with galvanostatic acceleration (PCGA) tests have been performed up to 5 cycles for different samples using a potential step of 4 mV and a current threshold of C/50 compared to the theoretical capacity (10 mAg^{-1}) to explore the electrode reaction mechanism in quasi thermodynamic behaviour.

Electrochemical impedance spectroscopy data (EIS) have been acquired using Swagelok cells (3 electrode configuration) assembled with the same working electrode used for the preparation of the CR2032 coin cells, and Na discs as counter and reference electrode. EIS spectra have been acquired on a VMP3 BioLogic with a sinus amplitude of 10 mV, and frequencies ranging from 1 MHz to 100 mHz.

RAMAN measurements

Micro-Raman measurements were carried out by a confocal labRAM (Horiba Jobin-Yvon) spectrometer, operating in backscattering configuration with a focal layer thickness of few microns. A helium–neon laser line at 632.8 nm was used as exciting source with spectral resolution of about 2 cm^{-1}. The scattered light was detected by a charge coupled device (CCD-Sincerity, JobinYvon). A microscope (Olympus BX40) was used to focus the excitation on the samples and to collect the scattered radiation, by a Long Working Distance 50x objective with a numerical aperture of 0.60, with a resulting sampled areas of ~5 μm in diameter, and a laser power on the sample of <1 mW. During operando Raman experiments, an EL-CELL ECC-Opto-Std test cell in Raman configuration was assembled in its sandwich setup, using metallic Na as counter electrode, NaClO$_4$ 1 M in PC with 2% FEC as electrolyte and the same mixture of FTO:binder:C reported previously prepared on Al mesh current collector as cathode (38–45 mg of active material deposited for each electrode). Focus position have been checked before the acquisition of each measure. Errors from defocussing due to contraction/expansion of the active material during electrochemical test does not exceed 5% of the signal intensity. Acquisition times were set in the range 30–600 s, ensuring an acceptable signal-to-noise ratio and a sufficiently fast measure with respect to changes in the charging/discharging current measurements.

All the samples prepared and cited in the following discussion are reported in Table S1 together with the labels used in the discussion and the experimental conditions considered for the preparation.

Conflict of Interest

The authors declare no conflict of interest.

[1] C. Zhao, Y. Lu, J. Yue, D. Pan, Y. Qi, Y.-S. Hu, L. Chen, *J. Energ. Mater.* **2018**, *27*, 1584–1596.
[2] X. Zheng, C. Bommier, W. Luo, L. Jiang, Y. Hao, Y. Huang, *Energy Storage Mater.* **2019**, *16*, 6–23.
[3] F. Li, Z. Wei, A. Manthiram, Y. Feng, J. Ma, L. Mai, *J. Mater. Chem. A* **2019**, 9406–9431.
[4] S. Mukherjee, S. B. Mujib, D. Soares, G. Singh, *Materials* **2019**, *12*, 1952.
[5] X. Pu, H. Wang, D. Zhao, H. Yang, X. Ai, S. Cao, Z. Chen, Y. Cao, *Small* **2019**, *1805427*, 1–33.
[6] T. Tao, A. M. Glushenkov, M. M. Rahman, Y. Chen, *Electrochim. Acta* **2013**, *108*, 127–134.
[7] C. Ding, T. Nohira, R. Hagiwara, *J. Power Sources* **2018**, *388*, 19–24.
[8] L. Yu, J. Liu, X. Xu, L. Zhang, R. Hu, J. Liu, L. Ouyang, L. Yang, M. Zhu, *ACS Nano* **2017**, *11*, 5120–5129.

[9] T. Tao, A. M. Glushenkov, H. Liu, Z. Liu, X. J. Dai, H. Chen, S. P. Ringer, Y. Chen, *J. Phys. Chem. C* **2011**, *115*, 17297–17302.

[10] A. Puthirath Balan, S. Radhakrishnan, R. Kumar, R. Neupane, S. K. Sinha, L. Deng, C. A. De Los Reyes, A. Apte, B. M. Rao, M. Paulose, R. Vajtai, C. W. Chu, G. Costin, A. A. Martì, O. K. Varghese, A. K. Singh, C. S. Tiwary, M. R. Anantharaman, P. M. Ajayan, *Chem. Mater.* **2018**, *30*, 5923–5931.

[11] C. Chen, F. Giovannelli, M. Zaghrioui, L. Perriere, F. Delorme, *Mater. Chem. Phys.* **2017**, *198*, 1–6.

[12] S. Guo, J. Liu, S. Qiu, Y. Wang, X. Yan, N. Wu, S. Wang, Z. Guo, *Electrochim. Acta* **2016**, *190*, 556–565.

[13] D. Gu, Y. Qin, Y. Wen, L. Qin, H. J. Seo, *J. Taiwan Inst. Chem. Eng.* **2017**, *78*, 431–437.

[14] J. Ru, Y. Hua, C. Xu, J. Li, Y. Li, D. Wang, K. Gong, R. Wang, Z. Zhou, *Ceram. Int.* **2014**, *40*, 6799–6805.

[15] A. T. Raghavender, N. Hoa Hong, K. Joon Lee, M. H. Jung, Z. Skoko, M. Vasilevskiy, M. F. Cerqueira, A. P. Samantilleke, *J. Magn. Magn. Mater.* **2013**, *331*, 129–132.

[16] P. Srinivas, A. S. Kumar, P. D. Babu, A. K. Bhatnagar, *J. Supercond. Novel Magn.* **2018**, *31*, 1189–1197.

[17] U. S. Geological Survey, *Mineral Commodity summaries 2019* **2019**.

[18] Y. Liu, T. Qi, J. Chu, Q. Tong, Y. Zhang, *Int. J. Miner. Process.* **2006**, *81*, 79–84.

[19] L. H. Lalasari, R. Subagja, A. H. Yuwono, F. Firdiyono, S. Harjanto, B. Suharno, *Adv. Mater. Res.* **2014**, *789*, 522–530.

[20] R. J. Harrison, S. A. T. Redfern, *Phys. Chem. Miner.* **2001**, *28*, 399–412.

[21] M. J. Gázquez, J. P. Bolívar, R. Garcia-Tenorio, F. Vaca, *Mater. Sci. Appl.* **2014**, *05*, 441–458.

[22] H. Sun, J. Wang, X. Dong, Q. Xue, *Metall. Int.* **2012**, *17*, 49–56.

[23] W. Phoohinkong, S. Pavasupree, A. Wannagon, K. Boonyarattanakalin, W. Mekprasart, W. Pecharapa, *Surf. Rev. Lett.* **2018**, *1840006*, 1–11.

[24] N. D. H. Arachchi, G. S. Peiris, M. Shimomura, P. M. Jayaweera, *Hydrometallurgy* **2016**, *166*, 73–79.

[25] S. Y. Mao, X. X. Ren, Z. H. Zhou, *Jiegou Huaxue* **2008**, *27*, 553–557.

[26] P. M. Jardim, L. Mancic, B. A. Marinkovic, O. Milosevic, F. Rizzo, *Cent. Eur. J. Chem.* **2011**, *9*, 415–421.

[27] M. T. Klepka, K. Lawniczak-Jablonska, A. Wolska, M. Jablonski, *J. Electron Spectrosc. Relat. Phenom.* **2010**, *182*, 85–89.

[28] S. Hirano, M. G. M.U Ismail, S. Somiya, *Mater. Res. Bull.* **1976**, *8*, 1023–1030.

[29] G. H. Du, Q. Chen, R. C. Che, Z. Y. Yuan, L. M. Peng, *Appl. Phys. Lett.* **2001**, *79*, 3702–3704.

[30] R. Ma, Y. Bando, T. Sasaki, *Chem. Phys. Lett.* **2003**, *380*, 577–582.

[31] H. Miao, X. Hu, Y. Shang, D. Zhang, R. Ji, E. Liu, Q. Zhang, Y. Wang, J. Fan, *J. Nanosci. Nanotechnol.* **2012**, *12*, 7927–7931.

[32] E. Morgado, M. A. S. De Abreu, G. T. Moure, B. A. Marinkovic, P. M. Jardim, A. S. Araujo, *Chem. Mater.* **2007**, *19*, 665–676.

[33] C. W. Peng, M. Richard-Plouet, T. Y. Ke, C. Y. Lee, H. T. Chiu, C. Marhic, E. Puzenat, F. Lemoigno, L. Brohan, *Chem. Mater.* **2008**, *20*, 7228–7236.

[34] A. Nakahira, W. Kato, M. Tamai, T. Isshiki, K. Nishio, H. Aritani, *J. Mater. Sci.* **2004**, *39*, 4239–4245.

[35] M. Shirpour, J. Cabana, M. Doeff, *Energy Environ. Sci.* **2013**, *6*, 2538–2547.

[36] T. Sasaki, M. Watanabe, Y. Komatsu, Y. Fujiki, *Inorg. Chem.* **1985**, *24*, 2265–2271.

[37] L. F. Que, F. Da Yu, K. W. He, Z. B. Wang, D. M. Gu, *Chem. Mater.* **2017**, *29*, 9133–9141.

[38] L. Que, Z. Wang, F. Yu, D. Gu, *J. Mater. Chem. A* **2016**, *4*, 8716–8723.

[39] B. F. Naylor, *J. Am. Chem. Soc.* **1945**, *67*, 2120–2122.

[40] G. Longoni, M. Fiore, J.-H. Kim, Y. H. Jung, D. Kyung Kim, C. M. Mari, R. Ruffo, *J. Power Sources* **2016**, *332*, 42–50.

[41] D. Nayak, S. Puravankar, S. Ghosh, V. Adyam, *Ionics* **2019**, *25*, 5857–5868.

[42] G. Carbonari, F. Maroni, S. Gabrielli, A. Staffolani, R. Tossici, A. Palmieri, F. Nobili, *ChemElectroChem.* **2019**, *6*, 1915–1920.

[43] L. Que, Z. Wang, F. Yu, D. Gu, *J. Mater. Chem. A* **2016**, *4*, 8716–8723.

[44] L.-F. Que, F.-D. Yu, K.-W. He, Z.-B. Wang, D.-M. Gu, *Chem. Mater.* **2017**, *29*, 9133–9141.

[45] A. Rudola, K. Saravanan, C. W. Mason, P. Balaya, *J. Mater. Chem. A* **2013**, *1*, 2653–2662.

[46] L. Zhang, H. B. Wu, X. W. D. Lou, *Adv. Energy Mater.* **2014**, *4*, 1300958.

[47] S. Fang, D. Bresser, S. Passerini, *Adv. Energy Rev.* **2020**, *10*, 1902485, 1–21.

[48] D. Puthusseri, M. Wahid, S. Ogale, *ACS Omega* **2018**, *3*, 4591–4601.

[49] J.-H. Kim, D. K. Kim, *J. Korean Ceram. Soc.* **2018**, *55*, 307–324.

[50] Y. Mei, Y. Huang, X. Hu, *J. Mater. Chem. A* **2016**, *4*, 12001–12013.

[51] S. Lou, Y. Zhao, J. Wang, G. Yin, C. Du, X. Sun, *Small* **2019**, *15*, 1904740, 1–44.

[52] Y. Wang, W. Zhu, A. Guerfi, C. Kim, K. Zaghib, *Front. Energy Res.* **2019**, *7*, 28, 1–12.

[53] S. Santangelo, M. Fiore, F. Pantò, S. Stelitano, M. Marelli, P. Frontera, P. Antonucci, G. Longoni, R. Ruffo, *Solid State Ionics* **2017**, *309*, 41–47.

[54] M. Fiore, G. Longoni, S. Santangelo, F. Pantò, S. Stelitano, P. Frontera, P. Antonucci, R. Ruffo, *Electrochim. Acta* **2018**, *269*, 367–377.

[55] V. Modafferi, M. Fiore, E. Fazio, S. Patanè, C. Triolo, S. Santangelo, R. Ruffo, F. Neri, M. G. Musolino, *Modell. Meas. Control B* **2018**, *87*, 129–134.

[56] A. G. Miller, J. W. Macklin, *J. Phys. Chem.* **1985**, *89*, 1193–1201.

[57] P. Cao, J. Yao, B. Ren, R. Gu, Z. Tian, *J. Phys. Chem. B* **2002**, *106*, 10150–10156.

[58] A. M. Hofmeister, *Eur. J. Mineral.* **1993**, *5*, 281–295.

[59] A. Fau, O. Beyssac, M. Gauthier, P. Y. Meslin, A. Cousin, K. Benzerara, S. Bernard, J. C. Boulliard, O. Gasnault, O. Forni, R. C. Wiens, M. Morand, P. Rosier, Y. Garino, S. Pont, S. Maurice, *Spectrochim. Acta Part B* **2019**, *160*, 105687, 1–14.

[60] B. Reynard, D. C. Rubie, *Am. Mineral.* **1996**, *81*, 1092–1096.

[61] A. Wang, K. E. Kuebler, B. L. Jolliff, L. A. Haskin, *Am. Mineral.* **2004**, *89*, 665–680.

[62] X. Hou, C. Li, H. Xu, L. Xu, *Nano Res.* **2017**, *10*, 3585–3595.

[63] B. Koo, H. Kim, Y. Cho, K. T. Lee, N. Choi, J. Cho, *Angew. Chem.* **2012**, *35*, 8762–8767.